

Article

Photocatalytic Activity of MoS₂ Nanoflower-Modified CaTiO₃ Composites for Degradation of RhB under Visible Light

Minghan Luo ^{1,2} , Jiaying Xu ¹ , Wenjie Xu ¹, Yu Zheng ¹, Gongde Wu ^{1,2,*} and Taeseop Jeong ³¹ School of Environmental Engineering, Nanjing Institute of Technology, Nanjing 211167, China² Energy Research Institute, Nanjing Institute of Technology, Nanjing 211167, China³ Department of Environmental Engineering, Chonbuk National University, Chonbuk 561-756, Republic of Korea

* Correspondence: wugongde@njit.edu.cn

Abstract: Nanoflower-like MoS₂ deposited on the surface of rectangular CaTiO₃ (CTO) was designed and synthesized via a simple template-free strategy. Through SEM, TEM, and other characterization methods, the MoS₂ nanoflowers were confirmed to be well deposited on the surface of CTO. LED was used as the visible light source, and rhodamine B (RhB) in an aqueous solution was used as the model pollutant to assess the photodegradation activity of the samples. The results showed that the MoS₂/CaTiO₃ (MCTO) composite significantly improved the photocatalytic degradation of rhodamine B (RhB) in water, compared with a single CTO, and with the MCTO-2 composite photocatalysts, 97% degradation of RhB was achieved in 180 min, and its photocatalytic activity was about 5.17 times higher than that of the bare CTO. The main reasons for enhancing photocatalytic performance are the strong interaction between the nanoflower-like MoS₂ and rectangular CTO, which can lead to the effective separation of electron transfer and photoexcited electron–hole pairs in MCTO composites. This work provides a new notion for researching an effective method of recycling catalytic materials.

Keywords: MoS₂; CaTiO₃; RhB; perovskite

Citation: Luo, M.; Xu, J.; Xu, W.; Zheng, Y.; Wu, G.; Jeong, T. Photocatalytic Activity of MoS₂ Nanoflower-Modified CaTiO₃ Composites for Degradation of RhB under Visible Light. *Nanomaterials* **2023**, *13*, 636. <https://doi.org/10.3390/nano13040636>

Academic Editor: Vincenzo Vaiano

Received: 8 January 2023

Revised: 24 January 2023

Accepted: 26 January 2023

Published: 6 February 2023



Copyright: © 2023 by the authors. Licensee MDPI, Basel, Switzerland. This article is an open access article distributed under the terms and conditions of the Creative Commons Attribution (CC BY) license (<https://creativecommons.org/licenses/by/4.0/>).

1. Introduction

In recent years, with rapid industrialization and urbanization due to the advancement of technology, the problem of treating a large amount of wastewater generated has become one of the most challenging issues worldwide. In particular, the biodegradability of the remaining pollutants in polluted wastewater is greatly reduced after mechanical, physical, chemical, and biological treatment. However, this process requires the development of more economical and efficient methods to treat refractory pollutants. Semiconductor photocatalysis, which uses light-activated materials to generate highly reactive radicals and completely mineralize with the adsorbed pollutants, is a novel, advanced oxidation technology with many advantages, including a fast reaction rate and no secondary pollution. The core of photocatalysis technology lies in the photocatalyst, and a high-performance catalyst can improve the rate and selectivity of basic chemical reactions. Therefore, designing suitable photocatalysts will advance the use of current photocatalytic materials. Perovskite materials, with a wide bandgap and suitable electrochemical potential, are the preferred choice [1].

Perovskites have received widespread attention for environmental, pharmaceutical, catalytic, sensor, and other electronic applications because of their unique energy band structure and stable physical and chemical properties, among many other advantages [2–8]. Perovskite-type photocatalysts are also of great significance in the field of photocatalysis. Various perovskite material systems have been extensively studied. However, their wide bandgap, low quantum efficiency, and the disadvantage of powder catalyst recovery have

restricted the extensive application of perovskite materials in the field of photocatalysis [6–8]. Various methods such as hydrothermal, sol–gel, and solid-phase reactions [9–12] can prepare perovskite materials with different morphologies of nanoparticles, nanorods, nanoflowers, and nanobelts, and they have shown excellent capabilities in the photocatalytic degradation of pollutants [3,13,14]. Xu et al. [15] reported the use of Halide perovskite quantum dots as novel photocatalysts to convert CO₂ into solar fuels in nonaqueous media. Under simulated illumination, the CsPbBr₃ QDs generated electrons and catalyzed CO₂ reduction with a selectivity of over 99.3%. Zhe et al. [16] introduced lead halide perovskite (CsPbBr₃) nanocrystals as band-edge-tunable photocatalysts for efficient photoinduced electron/energy transfer-reversible addition–fragmentation chain transfer polymerization, which was successfully conducted using a broad range of irradiation sources ranging from blue to red light (460 to 635 nm), resulting in polymer products with narrow dispersity and a high degree of chain-end fidelity. Zhu et al. [17] reported that lead-free bismuth halide perovskite nanocrystals encapsulated by covalent organic frameworks demonstrated good water processability, which facilitated the generation and transportation of photoinduced charge carriers. The characteristics of CTO are somewhat different from other commonly used photocatalytic materials, with its more negative conduction band and a more positive valence band, with a theoretically forbidden bandwidth of 3.5 eV. Consequently, its strong photogenerated electron–hole reduction and oxidation ability are confined to UV light conditions, and thus, it cannot degrade organic pollutants in sunlight. Many researchers have developed strategies to broaden the photoresponsive region and limit the interceptor’s fast complexation to improve photocatalysts’ activity [13–18]. For example, Zhang et al. [19] co-doped CTO particles with Ag⁺ and La³⁺ and showed that the absorption of visible light by CTO became stronger, which enabled CTO particles to split water for hydrogen production under visible light. Yan et al. [20] prepared CTO in nanorectangular cubes using P25 as the titanium source under hydrothermal conditions and further modified Au nanoparticles on the surface to form heterojunctions to enhance their photocatalytic degradation of RhB pollutants. Schuerings et al. [21] deposited CTO nanoflakes on the surface of g-C₃N₄ nanoflakes using a facile hybrid method to construct appropriate energy band positions that greatly extend the light absorption range (UV and visible-light regions), promote the transfer of photogenerated charges, and inhibit the rapid recombination of electron–hole pairs, thereby improving photocatalytic performance. In addition, a representative of transition metal sulfides-MoS₂ can be a suitable co-catalyst for the photocatalytic degradation of organic pollutants because of its narrow bandgap, large number of active sites, and large specific surface area [22]. The effective combination of these two substances into heterogeneously structured catalyst materials will better promote the efficient application of photocatalytic materials in various fields. For example, Jiang et al. [18] used a hydrothermal method to construct a novel Z-scheme MoS₂/CTO heterostructure with MoS₂ nanospheres tightly anchored on the surface of macroporous CTO cubes, and compared with single MoS₂ and CTO, the Z-scheme MoS₂/CTO heterostructure showed significantly enhanced photocatalytic performance in hydrogen generation and the degradation of antibiotics in water. The main reason for the enhanced photocatalytic performance is the Z-scheme electron transport mechanism and the strong interaction between the MoS₂ nanospheres and multilayer hollow CTO cubes. The Z-scheme MoS₂/CTO heterostructure with better charge carrier separation, faster charge transfer, and longer photogenerated charge lifetime was found to contribute to enhanced photocatalytic activity using photoelectrochemical analysis. Liu et al. [23] prepared 2D petal-like MoS₂/CTO nanocomposites modified with MoS₂ flakes using a simple, two-step hydrothermal method and found that the prepared materials have superior photocatalytic stability and significantly enhanced hydrogen production efficiency by about 30 times compared with unmodified CTO. Moreover, the modification of these petal-shaped MoS₂ nanoflakes can exhibit a larger specific surface area compared with nanospheres, which can absorb more light energy and contribute to the transport of photoelectrons. This improvement can be attributed mainly to the lower Fermi energy level of MoS₂ that can trap photoelectrons for improved charge carrier transfer. In

addition, flake nanostructures can enhance photocatalytic HER performance by providing sufficient active sites and shortening reaction times.

Photocatalysis is a method of material transformation by light energy and a chemical reaction of a substance produced by the combined action of light and a catalyst. The photocatalytic activity of a substance is closely related to the electronic layer configuration of the atoms that make up the substance, and its energy band structure determines its photocatalytic properties. In addition, in practice, when photocatalyst powder materials for wastewater purification are used, a large amount of powder suspended in the water causes additional problems such as secondary pollution and material loss, which limits their practical application for wastewater purification. Therefore, recycling photocatalytic materials before treating wastewater should be considered. In this paper, we designed and synthesized composites with nanoflower-like MoS₂ deposited on the surface of rectangular CTO using a simple template-free strategy. As expected, the prepared loaded MoS₂/CTO composites had excellent photocatalytic performance for the degradation of RhB in water. This paper also aimed to provide an overview of the photocatalytic reaction performance of recyclable perovskite materials in water treatment in light of the recent advances in the development of photocatalysts to provide a favorable basis for future practical applications.

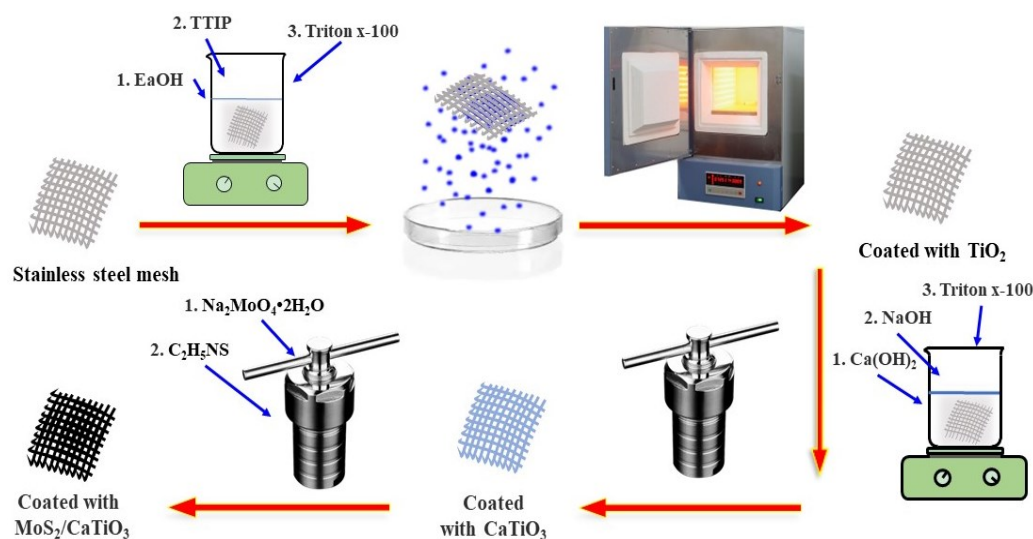
2. Experiment and Materials

2.1. Materials

Sodium molybdate dihydrate (Na₂MoO₄·2H₂O) (≥99%), thioacetamide (C₂H₅NS) (≥99%), titanium isopropoxide (C₁₂H₂₈O₄Ti, TTIP) (≥99%) and Triton x-100 were purchased from Shanghai Aladdin Biochemical Technology Co., Ltd. Calcium hydroxide (Ca(OH)₂) (≥96%) and sodium hydroxide (NaOH) (≥97%) were purchased from Nanjing WANQING chemical glassware and Instrument Co., Ltd. The 304 stainless steel mesh (300 mesh) for the experiment was purchased from Wuxi Sanlei Screen Products Co., Ltd. All the raw materials and other chemical reagents were of analytical grade and directly used without further purification.

2.2. Preparation of MoS₂/CTO Composites

MCTO composites were prepared in four steps. First, the purchased stainless steel mesh was pretreated, and then TiO₂ nanoparticles were loaded on the surface of the stainless steel mesh. Then, TiO₂ crystals were crystallized into the CTO calcium titanite material using the hydrothermal method. Finally, the nanoflake MoS₂ nanosheets were deposited on the surface of the CTO material to form the composites. Scheme 1 describes the specific composite material preparation process. (1) The stainless steel mesh was cleaned with acetone, ethanol, and water under ultrasonic conditions for 10 min and then dried and set aside. (2) Then, 3 mL of titanium isopropoxide (TTIP) was slowly added to 50 mL of anhydrous ethanol with magnetic stirring, and then 3 drops of Triton x-100 were added after 10 min, and stirring was maintained for 5 min. Then, the pretreated stainless steel mesh was placed into the above solution for 5 min with ultrasonic treatment and then transferred to an oven at 100 °C with support for evaporative self-assembly and condensation. The catalyst was repeatedly loaded four times, dried at room temperature for 1 h, and then placed in a 450 °C muffle furnace with a temperature rise rate of 5 °C/min for 2 h. (3) Next, 0.1 g of Ca(OH)₂ and 2M NaOH were added to 100 mL deionized water with magnetic stirring until completely dissolved. The above solution was then poured into a 100 mL reaction kettle and hydrothermally reacted at 120 °C for 24 h. (4) Sodium molybdate (Na₂MoO₄·2H₂O) and thioacetamide (C₂H₅NS) were dispersed into 100 mL of deionized water and magnetically stirred for 30 min. Then, the prepared loaded CTO material was placed into the above solution and transferred to the reactor for hydrothermal reaction at 200 °C for 24 h. Finally, it was cleaned and dried with deionized water and ethanol. The preparation conditions for the composites are shown in Table 1.



Scheme 1. Schematic diagram of the preparation process of the samples.

Table 1. Preparation conditions for the MCTO composites.

Condition	200 °C, 24 h, 80 mL			
Na ₂ MoO ₄ ·2H ₂ O	0.10	0.20	0.40	0.80
C ₂ H ₅ NS	0.18	0.36	0.72	1.44
Samples No.	MCTO-1	MCTO-2	MCTO-3	MCTO-4

2.3. Characterization Methodologies

To unveil the morphology and microstructure of the samples, scanning electron microscopy (SEM) and high-resolution transmission electron microscopy (HRTEM) with an energy-dispersive X-ray spectroscope (EDS) were performed to obtain the microstructure and morphology images of the as-prepared materials on a Regulus-8100 field-emission scanning electron microscope and a JEM-2100F field-emission transmission electron microscope. X-ray powder diffraction (XRD) was used to determine the crystalline structure of the samples on a D8 Advance X-ray diffractometer ($\lambda_{\text{Cu-K}\alpha} = 0.154 \text{ nm}$). An AXIS multi-functional X-ray photoelectron spectrometer was used for the X-ray photoelectron spectroscopy (XPS) measurement elements to reveal the elements' chemical states. Ultraviolet–visible (UV–Vis) diffuse reflectance spectroscopy (DRS) was employed to characterize the optical absorption and bandgap energy of the samples, measured on a Cary 500 double-beam UV–Vis spectrophotometer using BaSO₄ as a reference.

2.4. Photocatalytic Test Procedure

The visible light photocatalytic performances of CTO and MCTO1–MCTO4 were evaluated by the degradation of RhB in three different pH aqueous solutions containing a concentration of 1 mg/L RhB and 0.01 g catalyst in 300 mL glass vessels. First, the suspension was vigorously stirred in the dark for 30 min to achieve adsorption–desorption equilibrium between the RhB and the catalysts, and then it was irradiated under a 15W LED lamp light source (NVC-6500K, NVC Group, Chongqing, China). The dye solution catalytic decolorization is a pseudo-first-order reaction, and the degradation rate is estimated using Equation (1) [21]:

$$\text{Degradation (\%)} = (1 - C_t/C_0) \times 100\% \quad (1)$$

where C_t and C_0 are the dye's concentration at time t and initial concentration, respectively. To test the residual RhB concentration in the process of photocatalytic degradation, 3 mL of the reaction solution was taken at different time periods and transferred to a UV–Vis spectrophotometer to measure the absorbance (λ_{RhB}) at 554 nm.

3. Results and Discussion

3.1. Characterization

Figure 1a shows that the diffraction peaks located at 25.84, 29.81, 35.86, 43.17, and 45.16 correspond to the (111), (121), (112), (003), and (212) crystal planes of the CTO sample. In addition, with the addition of MoS₂ nanoflowers, new diffraction peaks were observed at 14.49, 29.21, 34.17, 38.28, 41.13, 44.45, 48.05, 52.01, 58.35, 60.47, 66.58, 68.74, 73.87, and 76.19, with significant changes relative to CTO. Upon comparison, the positions correspond to the (003), (006), (101), (012), (104), (015), (009), (107), (018), (110), (113), (116), (021), (205), and (119) crystal planes of the MoS₂ PDF card. The intensity of the diffraction peaks is not very obvious because of different conditions such as crystallinity, thickness, and incorporation. However, the presence of MoS₂ can be confirmed by other testing means, such as the HRTEM image. Moreover, the presence of the corresponding elements in appropriate proportions in the prepared material can be well demonstrated in the EDS spectra of Figure 1b. The three strong peaks evident in both samples in the figure correspond to the diffraction peaks of crystalline surfaces composed of several elements such as Fe, Ni, and Cr. This phenomenon makes the diffraction peaks of the MCTO materials prepared on stainless steel substrates less intense.

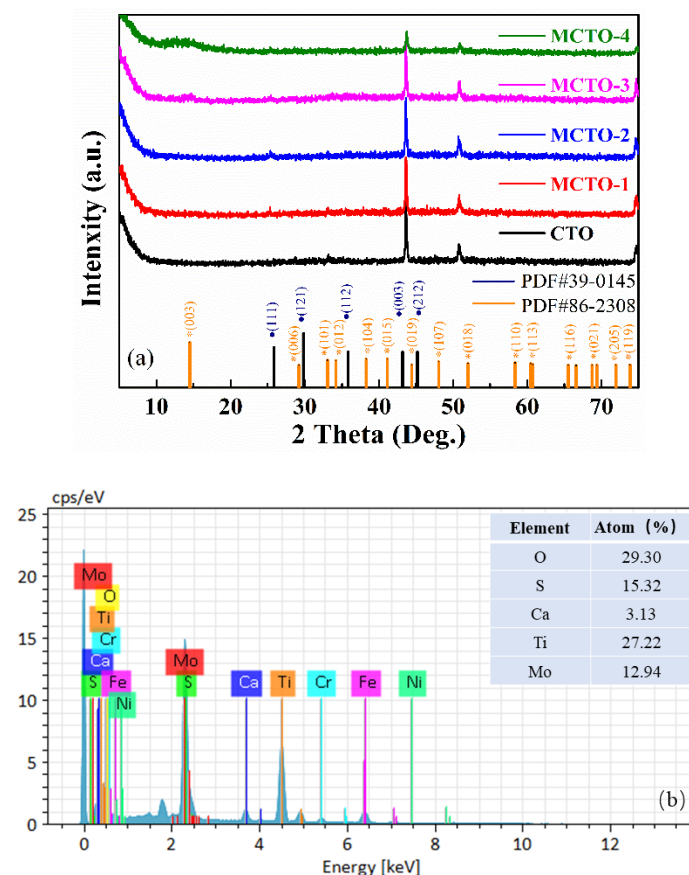


Figure 1. (a) X-ray diffraction patterns of samples obtained at 450 °C for 2 h; (b) EDS pattern of MCTO-2 sample.

Figure 2 shows the scanning electron microscope (SEM) images of the prepared samples. The prepared materials are well loaded on the smooth stainless steel mesh surface (Figure 2a,b), and the loading is relatively uniform and firm (Figure 2c,d). In this study, TiO₂ microspheres with an average diameter of about 300 nm (Figure 2e) were produced via in situ solvent evaporation and hydrolysis, and CTO (Figure 2f) was synthesized using the hydrothermal method. Finally, the hydrothermal method was used to synthesize different

masses of MoS₂ and CTO materials. The visible photocatalytic material MCTO (m-1–m-4 of Figure 2) was obtained.

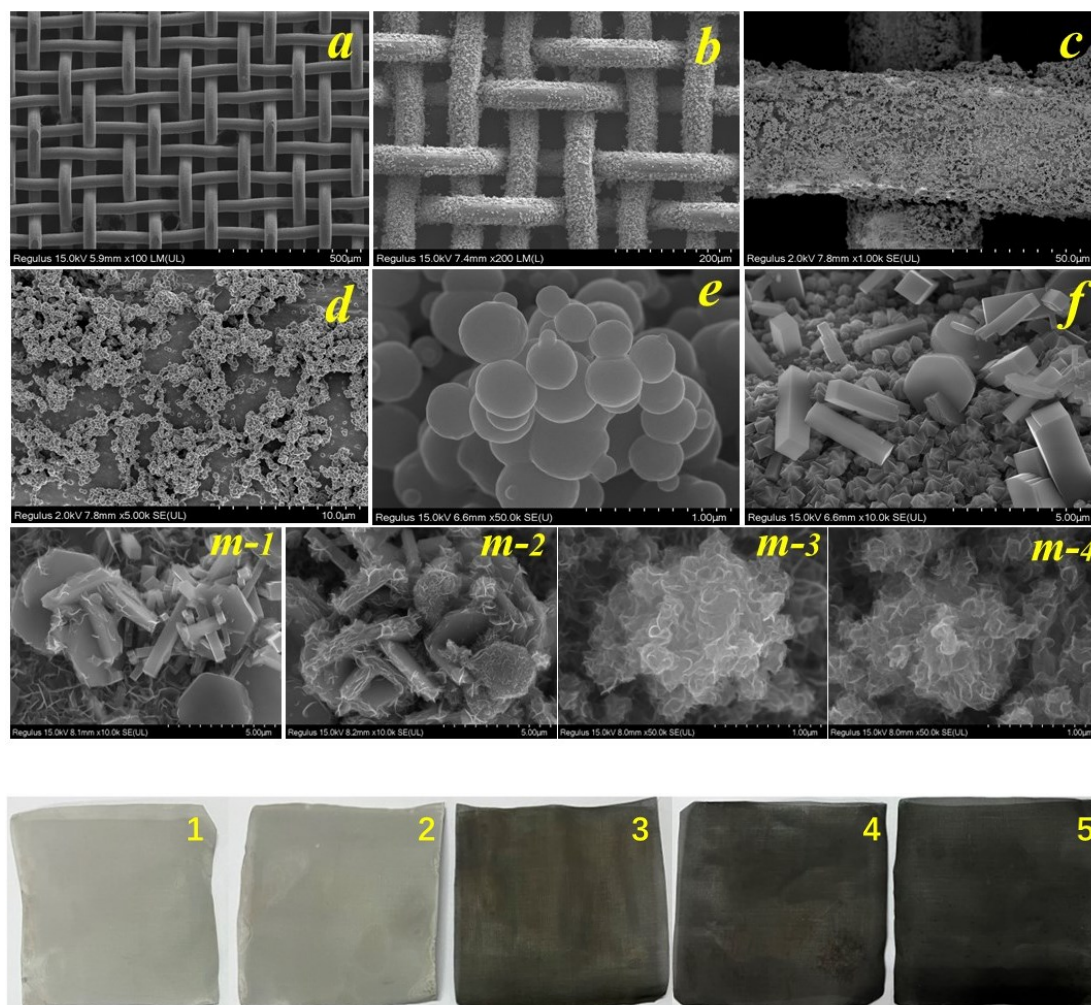


Figure 2. SEM of the samples. TiO₂ electron microscope pictures with different magnifications (a–e); as-prepared cubic CaTiO₃ (f); figures of different quality MoS₂ deposited on CaTiO₃ surface (m-1–m-4); actual figures of the prepared materials (1–5 of Figure 2 correspond to CTO, m-1, m-2, m-3, and m-4, respectively).

In conclusion, TiO₂ microspheres of different sizes from 100 to 500 nm were first produced in this experiment. The spherical TiO₂ was gradually recombined into cubic and polygonal CTO materials after a certain period of hydrothermal reaction by adding Ca ions to the aqueous solution, and the XRD and EDS spectra of the solutions were evaluated, as shown in Figure 1. For the further synthesis of MoS₂/CTO materials, the rectangular and polygonal CTO surfaces were deposited with nanoflower-like MoS₂ materials [1], which provided sufficient specific surface area and active sites for the photocatalytic degradation process. However, the coverage of the CTO increased with the increase in MoS₂, which may shield the function of the CTO and cause the existence of the CTO to lose its significance. The actual figures of the prepared material are shown in images 1–5 of Figure 2 and are consistent with the results observed in the SEM plots above.

Figure 3 shows the projection scanning electron microscopy (SEM) images of the surface of MoS₂ nanoflower material modified with rectangular bulk CTO. Figure 3 shows that the material's surface is covered by nanoflower-like flakes (Figure 3a,b), consistent with the appearance captured in the SEM images. The thickness of the nanoflower-like MoS₂ flakes modified on the surface of CTO is thin, and thus, the diffraction intensity in the

X-ray diffraction spectrum is also low, which is in agreement with Liu et al. [1]. Figure 3c,d are the HRTEM images of CTO and MoS₂ nanoflake materials. The crystal plane spacing of the two materials was 0.36 nm and 0.62 nm, respectively. Moreover, Figure 3e shows the HAADF and EDS mapping images, which exhibit all the elements of Ca, Ti, O, Mo, and S in the MCTO composites. It can be concluded from the above results that the MoS₂ nanoflower material was well deposited on the surface of the CTO material, which would cause the wide bandgap calcium titanate material to improve the absorption properties of its light energy to a great extent with the MoS₂ material. Ultimately, it was beneficial in improving photocatalytic degradation efficiency.

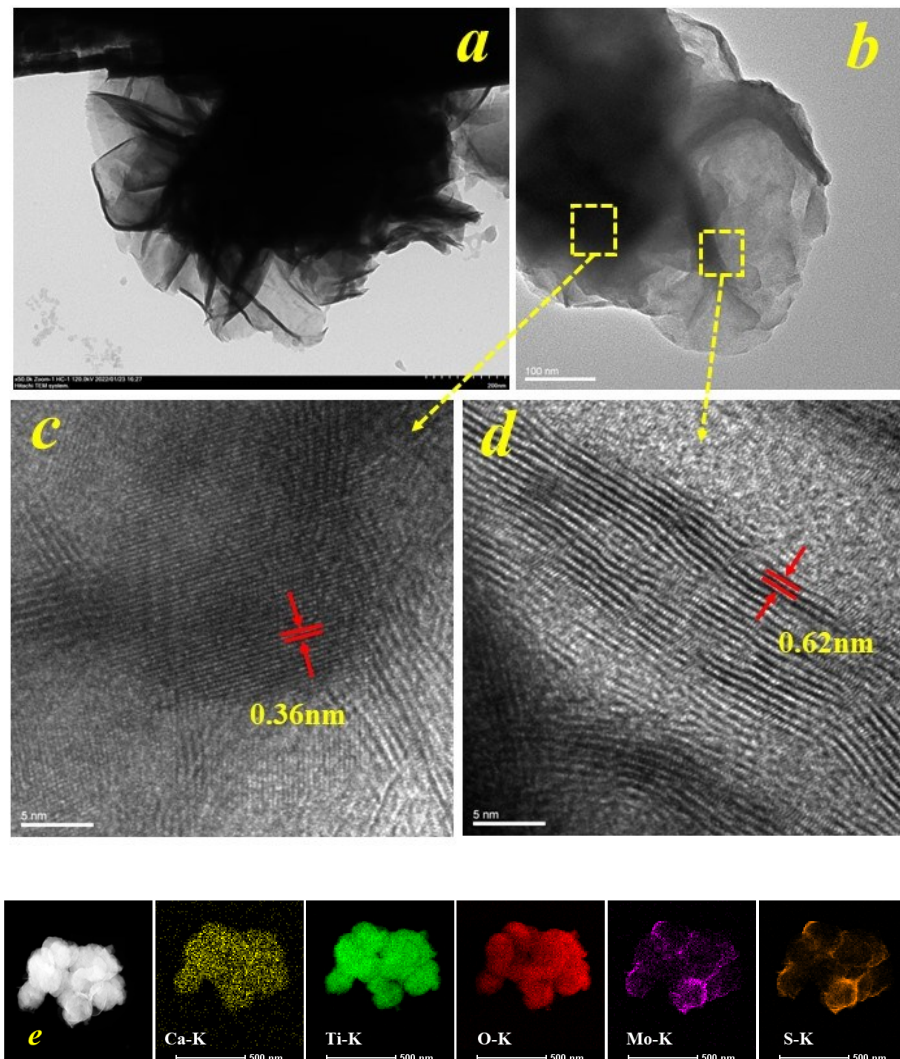


Figure 3. TEM of the MoS₂ modified CTO (MCTO-2), (a) TEM of the MCTO-2, (b) interface of the MCTO-2, (c) HRTEM of the CTO, (d) HRTEM of the MoS₂, and (e) HAADF and EDS mapping images of the MCTO-2.

Figure 4 shows the XPS images of CTO modified with MoS₂ nanoflowers. The presence of Ca, Ti, O, Mo, and S elements can be seen in the full spectrum of Figure 4a. In addition, the corresponding XPS patterns of each element are shown in Figure 4b–f. The peaks at 351.0 eV and 347.8 eV are attributed to Ca 2p_{1/2} and Ca 2p_{3/2}, respectively, as seen in the Ca 2p spectrum in Figure 4b [24]. Figure 4c, d show the XPS patterns of Ti 2p and O 1s. With Gaussian fitting, it can be determined that the peaks located at 465.8 eV and 459.8 eV are attributed to Ti 2p_{1/2} and Ti 2p_{3/2} of Ti⁴⁺, and the peaks located at 533.6 eV and 531.2 eV are attributed to the OH[−] and O^{2−} of surface-adsorbed water in the chalcocite structure [25].

The results of the above data indicate the successful preparation of chalcogenide CTO materials. The XPS patterns of Mo 3d and S 2p are shown in Figure 4e,f. Figure 4 shows that the peaks located at 232.2 eV, 229.1 eV, and 226.5 eV are attributed to Mo 3d_{3/2}, Mo 3d_{5/2}, and S 2s, respectively. These peaks originate from Mo⁴⁺, a part of the edge S nuclei in MoS₂ nanoflakes [23]. In addition, the peak located at 236.4 eV belongs to Mo⁶⁺ of the Mo-O bond because the exposed Mo atoms are bound to the O atoms in CTO, as some of the S atoms present on the surface of the MoS₂ nanoflakes may be stripped during the deposition process [23]. Moreover, the peaks at 163.1 eV and 162.0 eV are attributed to S 2p_{1/2} and S 2p_{3/2}, which are derived from the hybrid chemical bonding of S²⁻ and Mo-S [26]. The above results show that the MoS₂ nanoflowers material was successfully deposited on the surface of the CTO material.

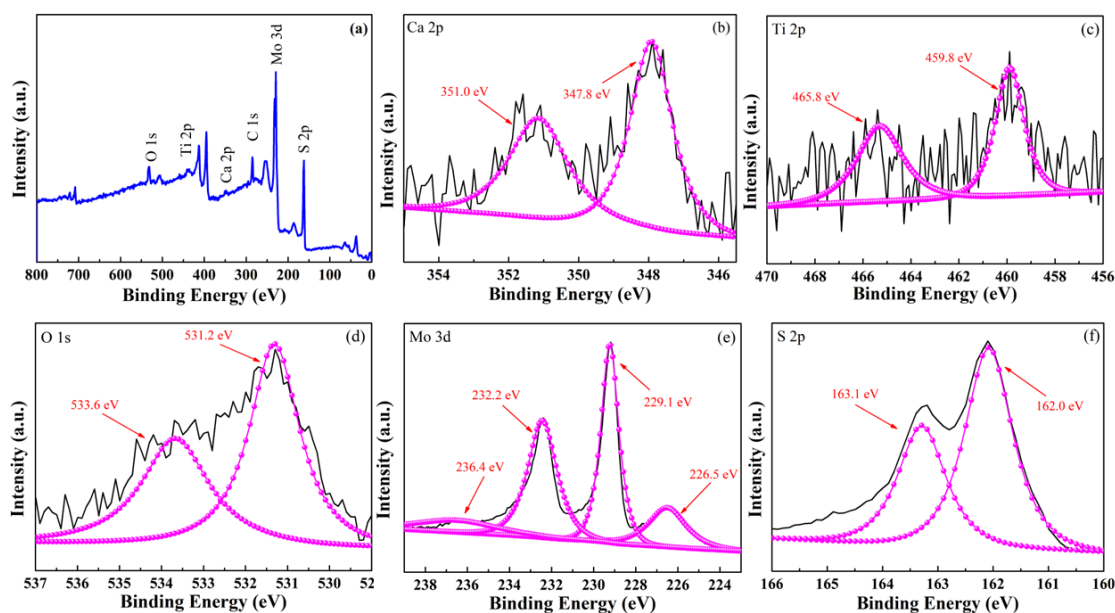


Figure 4. XPS of CTO and MCTO-2, (a) full curve, (b) Ca 2p spectrum, (c) Ti 2p spectrum, (d) O 1s spectrum, (e) Mo 3d spectrum, and (f) S 2p spectrum.

Figure 5a shows the UV–Vis absorption spectra of MCTO materials with different MoS₂ contents. As shown in the figure, the apparent absorption at about 380 nm is attributed to the intrinsic bandgap of TiO₂ [25], followed by a slight enhancement of light absorption by CTO. With the introduction of nanoflowered MoS₂, the material exhibited a significant absorption enhancement in the visible range, a feature attributed to the full spectral response of the MoS₂ material exposing more active sites and increasing light utilization [23]. The interaction between MoS₂ and CTO could induce a synergistic effect to increase the light-trapping ability and enhance the photocatalytic activity of the composite catalyst. In particular, although MCTO-4 had the highest visible light absorption intensity, MCTO-2 had the highest photocatalytic degradation performance, suggesting that the MoS₂ nanoflower material is more significant for the co-catalytic effect of CTO than its visible light absorption capacity and that an optimal ratio exists for the combination of the two. As the MoS₂ itself does not have a photocatalytic ability, the effect of excessive MoS₂ deposition can not only mask the photocatalytic degradation ability of CTO but can also have the effect of competing with visible light absorption. In addition, the excessive aggregation of MoS₂ on the CTO surface also reduces edge S atoms, which can also have a negative effect on photocatalytic degradation performance [1,23]. The relation between the absorption coefficient and bandgap energy for a direct gap semiconductor can be described by Equations (2)–(4) [4,27].

$$(\alpha h\nu)^2 = A(h\nu - E_g) \quad (2)$$

$$\alpha = (1/d)\ln(1/T) \quad (3)$$

$$E_g = 1240/\lambda_g \tag{4}$$

where E_g is the optical bandgap energy, $h\nu$ is the photon energy, A stands for the constant of the semiconductor, d is the transmittance, and T is the thickness. As shown in Figure 5b, the bandgap energies of the CTO and MCTO-1~MCTO-4 were calculated to be 3.15 eV, 3.13 eV, 3.06 eV, 2.89 eV, and 2.64 eV, respectively, indicating the combination of MoS₂ and CTO tremendously decreased the bandgap energy, enhancing the absorption and utilization of the light irradiation [18].

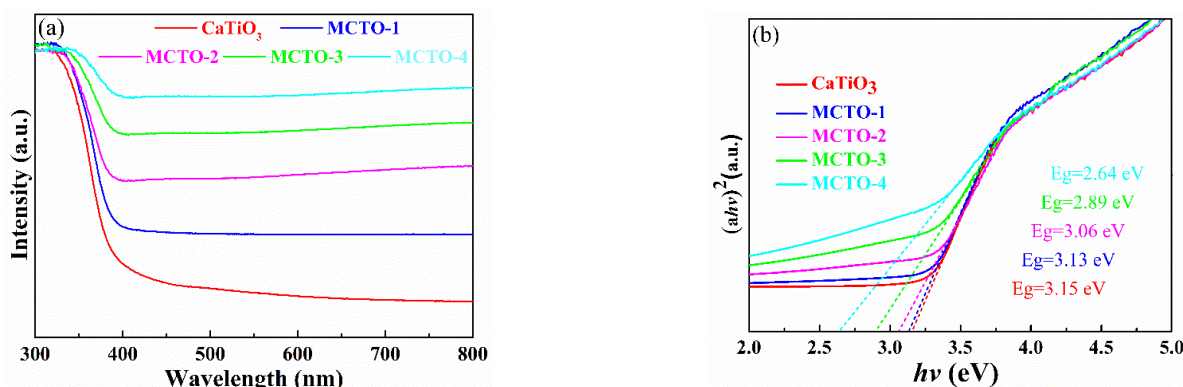


Figure 5. UV-Vis absorption spectra (a) and $(\alpha h\nu)^2$ plots (b) of the different MoS₂/CaTiO₃.

3.2. Photocatalytic Application

To examine the photocatalytic activity of synthesized MoS₂/CTO composites MCTO-1~MCTO-4 and CTO on RhB dye were studied under the influence of visible light. Figure 6a shows that the degradation rate of square-shaped CTO particles in RhB solution was 19% at 180 min, which showed weak degradation ability. The degradation efficiency of the RhB solution was also differentially influenced by the addition of MoS₂. According to our results, the degradation rate of the MCTO-2 sample reached 97% at 180 min, showing the most significant degradation effect; other samples, such as MCTO-1, MCTO-3, and MCTO-4, showed degradation rates of 32%, 78%, and 66%, respectively. Figure 6c also shows that the pH of different solutions had a considerable effect on the pollutant removal effect.

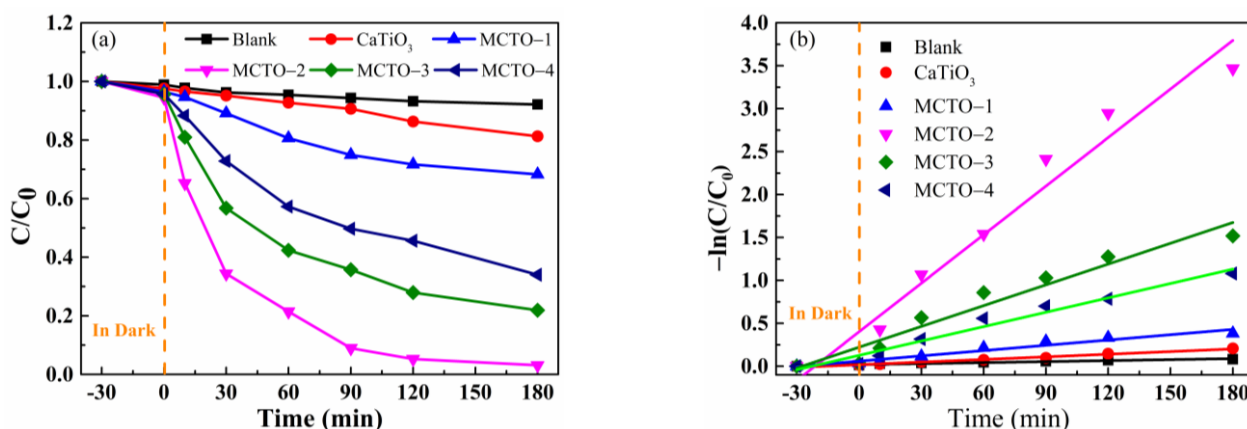


Figure 6. Cont.

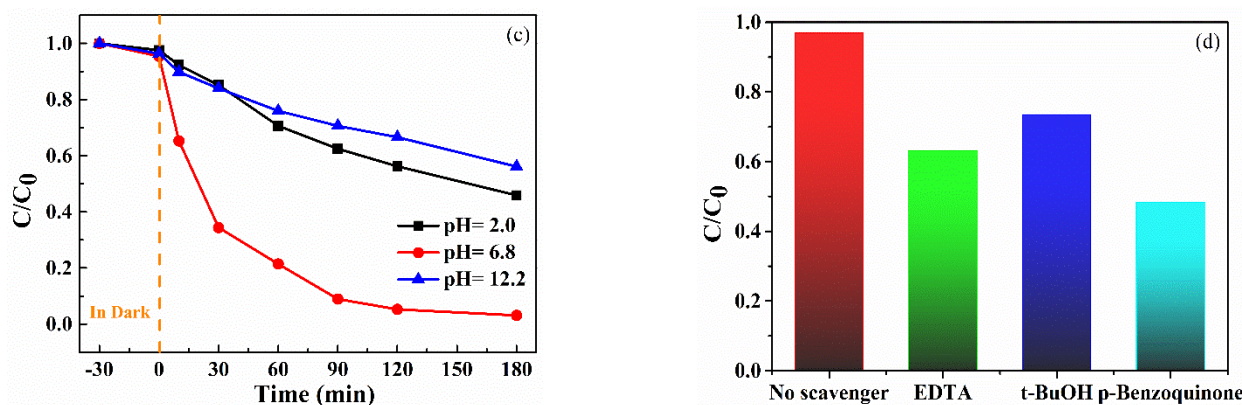


Figure 6. Photodegradation of RhB over CTO and MoS₂/CaTiO₃ composites (a) and kinetic plots (b), at different initial pH (c), and different scavengers (d) of the RhB degradation over the samples.

Figure 6b and Table 2 present the first-order kinetic fitting results and kinetic constants for the degradation of RhB solution by the sample catalysts. From this visible light degradation experiment, the addition of MoS₂ was found to significantly improve the utilization of visible light and accelerate the electron separation process and transmission efficiency, thereby effectively improving the photocatalytic degradation efficiency. Therefore, it is not hard to see that the addition of MoS₂ promoted photocatalytic activity, and different amounts of MoS₂ had different activities. This is because the black MoS₂ with a narrow bandgap can absorb more visible light energy and transfer the light energy to the CTO with a wide bandgap to improve the electron transition and reaction. However, excessive MoS₂ deposition can shield the transmission of light energy and inhibit the effective photocatalytic reaction. Therefore, there is an appropriate value for the amount of MoS₂ deposition. Too much or too little will have different effects on the photocatalytic reaction [28].

Table 2. First-order apparent rate constants (k) of different samples for RhB photodegradation.

Samples	Blank	CTO	MCTO-1	MCTO-2	MCTO-3	MCTO-4
Degradation (%)	7.87	18.75	31.72	96.88	78.07	66.01
K/min ⁻¹	0.0004	0.0011	0.0021	0.0189	0.0081	0.0056
R ²	0.944	0.987	0.943	0.954	0.941	0.965

To explore the detailed mechanism in the actual visible light catalytic reaction, the main active oxidation groups can be summarized as h⁺, ·O₂⁻, and ·OH [28]. In this paper, the species related to the degradation of RhB by MCTO composites were further investigated by capturing active groups. EDTA was added to the photocatalytic reaction as an h⁺ trapping agent, t-BuOH as ·OH trapping agent, and p-Benzoquinone as ·O₂⁻ trapping agent. The addition of scavengers inhibited photocatalytic degradation efficiency. After adding the different scavengers, the RhB degradation rates by MCTO composites presented different trends, as shown in Figure 6d. The photocatalytic efficiency of degradation RhB without adding a trapping agent was 96.88%. The degradation efficiencies after adding EDTA, t-BuOH, and p-Benzoquinone were 63.14%, 73.42%, and 48.35%, respectively, which confirmed that O₂⁻ was the crucial active species used for oxidation, and h⁺ and ·OH mainly played a synergistic role in the photocatalytic reaction. Therefore, it could be inferred that the active species affected the photocatalytic activity in the following order: O₂⁻ > h⁺ > OH.

Figure 7 shows that the stability of the photocatalytic material is another significant factor in evaluating degradation performance. During the continuous 900 min photocatalytic process (Figure 7a), MCTO-2 maintained reasonable stability and obtained a high average value (Figure 7b), which was very close to the initial degradation rate and could be considered a more desirable result. In addition, the RhB degradation performance

obtained from this study was further compared with other materials reported in Table 3. In addition, it has advantages regarding catalyst dosage, power consumption, and other factors. Introducing MoS₂ can effectively improve the photocatalytic performance and degradation stability of CTO. Therefore, the mechanism of MoS₂ in this system will be an issue worth further exploration.

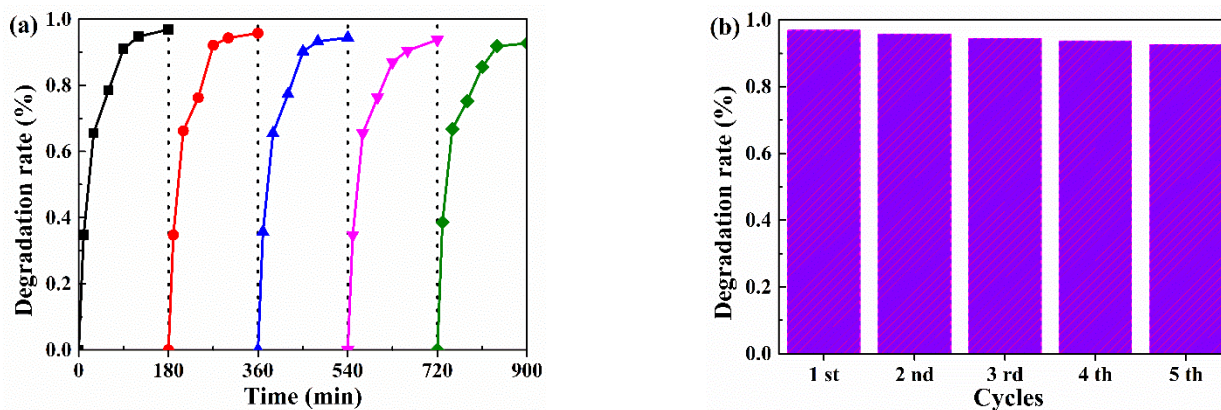


Figure 7. (a) The cycle curve of the MoS₂ modified CaTiO₃ (MCTO-2); (b) the histogram of the sample.

Table 3. Photocatalytic RhB performances of different photocatalysts.

Photocatalysts	C ₀ (mg/L)	Catalyst Dosage (mg)	Light Wavelength (λ)	Light Power	Degradation (%) min ⁻¹	Ref.
MoS ₂ /TiO ₂	9.6	Null	Simulated sunlight	500 W	76%/180 min	[28]
MoS ₂ /ZnO	4.8	150	Natural sunlight	300 W	100%/90 min	[29]
BiFeWO ₆ /MoS ₂	25	25	Visible-light	500 W	100%/75 min	[30]
MoS ₂ /WO ₃	10	100	Solar light	Null	98%/90 min	[24]
CaTiO ₃	3	100	UV bulbs	15 W	98%/300 min	[31]
CTO@BiOBr	5	100	Simulated sunlight	200 W	99%/30 min	[32]
CC@MoS ₂ -Ag ₃ PO ₄	5	10	Simulated daylight	300 W	96%/80 min	[33]
MoS ₂ /CaTiO ₃	1	25	LED lamp	15 W	97%/180 min	Our work

C₀: the initial concentration.

3.3. Proposed Photocatalytic Mechanism

Based on the above results, a possible photocatalytic mechanism of the MoS₂/CTO composite was investigated, which is shown in Scheme 2. The valence band is the highest range of electron energies in which electrons are normally present at absolute zero temperature. The following empirical equations were employed to calculate the VB and CB potentials:

$$E_{CB} = \chi - E^{\theta} - 0.5E_g \quad (5)$$

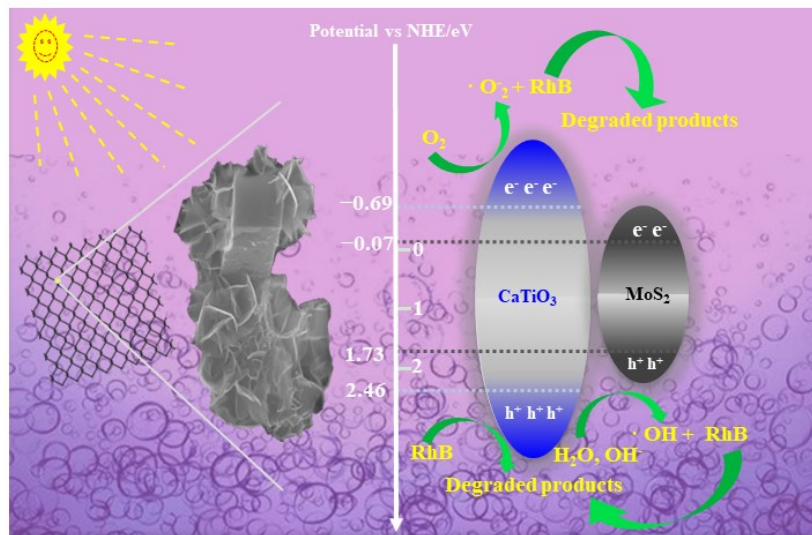
$$E_{VB} = E_{CB} + E_g \quad (6)$$

$$\chi = (E_{EA} + E_{ion})/2 \quad (7)$$

$$\chi = (\chi^1 \times \chi^2 \times \chi^3 \dots \times \chi^n)^{1/n} \text{ or } \chi = [\chi(A)^a \chi(B)^b \chi(C)^c]^{(1/a+b+c)} \quad (8)$$

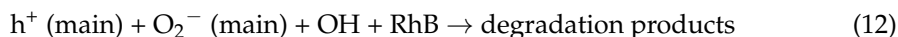
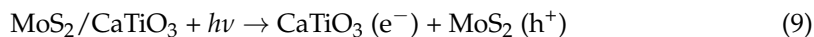
where χ is the absolute electronegativity (Mulliken) of the atom semiconductor, expressed as the geometric mean of the absolute electronegativity of the constituent atoms, which is defined as the arithmetic mean of the atomic electron affinity and the first ionization energy. E^{θ} is the energy of free electrons based on the hydrogen scale (4.50 eV), which is the kinetic energy of electrons, and E_g is the bandgap of the semiconductor. The E_{VB} , E_{CB} , and E_g are the valence potential, conduction band potential, and energy gap, respectively [24]. In this study, a set of codes was written in Python to calculate the positions of the valence

and conduction bands of CTO and MoS₂ for the above equations. The E_{VB} and E_{CB} edge potentials of CTO were calculated to be +2.46 eV and −0.69 eV, respectively, and those of MoS₂ were +1.73 eV or +1.43 eV and −0.07 eV or 0.23 eV, respectively.



Scheme 2. Photocatalytic RhB mechanism of the MoS₂/CTO.

The compounding of semiconductor materials with different bandgap structures is beneficial to electron transfer, which in turn promotes photogenerated electron–hole separation. It expands the absorption range of visible light, ultimately achieving the purpose of improving and enhancing the photocatalytic activity of semiconductor materials. Combining the above experimental results, Scheme 2 demonstrates the possible photocatalytic reaction mechanism and electron transfer behavior of MoS₂/CTO composites. When simulated sunlight irradiated the composites, the electrons on VB of MoS₂ and CTO were transferred to CB, leaving generated holes on their VB. The holes at this time could not only directly decompose RhB in water through oxidation but also decomposed H₂O molecules into highly oxidatively active hydroxyl radicals (OH). The electrons transferred from VB to CB reduced the dissolved O₂ in water to O₂[−] and degrade RhB again because the CB potential position of CTO (−0.69 eV) is more negative (−0.046 eV) than the CB potential of O₂/O₂[−] [18,21]. In conclusion, the active species ·O₂[−] and OH and h⁺ generated by electron transfer can oxidize RhB and eventually decompose it into small molecules, where h⁺ and O₂[−] are the most abundant active species [34]. The detailed equation is as follows:



4. Conclusions

In summary, recyclable loaded composites were made by depositing MoS₂ nanoflowers on the surface of rectangular CTO via in situ solvent evaporation self-assembly and hydrothermal method using a stainless steel mesh as the substrate. They were applied to the experiments of photocatalytic degradation of RhB solutions to investigate the effects of factors such as deposition amount, catalyst dosage, and catalytic time on the catalytic effect. The results showed that the efficiency of MCTO-2 material for the photocatalytic degradation of RhB was about 5.17 times higher than that of pure CTO material. A 97% degradation of RhB was achieved in 180 min under the conditions of 10 mg MCTO-2, 1 mg/L RhB, and a pH value of 6.8. The effective photocatalytic performance of the MCTO-

2 composites could be attributed to the composite construction and the in situ growth of MoS₂ on the rectangular CTO, which was confirmed by XRD, XPS, SEM, and HRTEM. The excellent photocatalytic performance of MCTO-2 for the degradation of RhB was also attributed to the strong interaction between the indirect bandgap structure of MoS₂ and the direct bandgap structure of CTO, which could effectively improve the wide spectrum response and charge separation. The application of recyclable composites to practical water treatment was attempted in this experiment. The experimental results and contents will provide a viable scientific basis for applying recyclable composites in practical solutions for water treatment.

Author Contributions: Conceptualization, G.W. and T.J.; methodology, M.L. and T.J.; validation, J.X. and W.X.; formal analysis, M.L. and J.X.; investigation, Y.Z. and W.X.; resources, M.L.; and J. X.; data curation, M.L. and J.X.; writing—original draft preparation, M.L.; writing—review and editing, M.L. and J.X.; visualization, W.X.; supervision, G.W. and T.J.; project administration, M.L. and J.X.; funding acquisition, T.J. All authors have read and agreed to the published version of the manuscript.

Funding: This research was funded by the Cooperation Fund of Energy Research Institute, Nanjing Institute of Technology (No. CXY201925), and The Natural Sciences Foundation of Nanjing Institute of Technology (NO. YKJ201847).

Institutional Review Board Statement: Not applicable.

Data Availability Statement: The data that support the findings of this study are available from the corresponding author upon reasonable request.

Acknowledgments: This work is supported by the Cooperation Fund of Energy Research Institute, Nanjing Institute of Technology (No. CXY201925), and The Natural Sciences Foundation of Nanjing Institute of Technology (NO. YKJ201847).

Conflicts of Interest: The authors declare no conflict of interest.

References

1. Liu, Y.; Pan, J.; Li, H.; Ou, W.; Li, S.; Zhao, W.; Wang, J.; Song, C.; Zheng, Y.; Li, C. The 2D petaloid MoS₂ lamellas modified cubic CaTiO₃ nanocomposites towards photocatalytic hydrogen production enhancement. *J. Alloy. Compd.* **2019**, *811*, 152067. [[CrossRef](#)]
2. Biegalski, M.; Qiao, L.; Gu, Y.; Mehta, A.; He, Q.; Takamura, Y.; Borisevich, A.; Chen, L. Impact of symmetry on the ferroelectric properties of CaTiO₃ thin films. *Appl. Phys. Lett.* **2015**, *106*, 162904. [[CrossRef](#)]
3. Zhuang, J.; Tian, Q.; Lin, S.; Yang, W.; Chen, L.; Liu, P. Precursor morphology-controlled formation of perovskites CaTiO₃ and their photo-activity for As (III) removal. *Appl. Catal. B Environ.* **2014**, *156–157*, 108–115. [[CrossRef](#)]
4. Oliveira, L.; Moura, A.; Port, F.; Nogueir, I.; Aguiar, E.; Sequinel, T.; Rosa, I.; Longo, E.; Varela, J. Influence of Cu-doping on the structural and optical properties of CaTiO₃ powders. *Mater. Res. Bull.* **2016**, *81*, 1–9. [[CrossRef](#)]
5. Oliveira, L.; Ramírez, M.; Ponce, M.; Ramajo, L.; Albuquerque, A.; Sambrano, J.; Longo, E.; Castro, M.; La Porta, F. Optical and gas-sensing properties, and electronic structure of the mixed-phase CaCu₃Ti₄O₁₂/CaTiO₃ composites. *Mater. Res. Bull.* **2017**, *93*, 47–55. [[CrossRef](#)]
6. Manjusha, P.; Bonamali, P. A review on CaTiO₃ photocatalyst: Activity enhancement methods and photocatalytic applications. *Powder Technol.* **2021**, *388*, 274–304.
7. Underwood, T.M.; Robinson, R.S. Adducing Knowledge Capabilities of Instrumental Techniques Through the Exploration of Heterostructures' Modification Methods. *Chemphyschem* **2022**, *23*, e202200241. [[CrossRef](#)]
8. Ariba, B.; Abdul, S.; Niaz Ahmad, N.; Sajjad, H. Muhammad Saeed Akhtar. Electrical transport properties and thermoelectric power studies of polyaniline–CaTiO₃ composites. *Polym. Bull.* **2022**. [[CrossRef](#)]
9. Han, C.; Liu, J.; Yang, W.; Wu, Q.; Yang, H.; Xue, X. Enhancement of photocatalytic activity of CaTiO₃ through HNO₃ acidification. *J. Photochem. Photobiol. A: Chem.* **2016**, *322–323*, 1–9. [[CrossRef](#)]
10. Xian, T.; Yang, H.; Huo, Y.; Ma, J.; Zhang, H.; Su, J.; Feng, W. Fabrication of Ag-decorated CaTiO₃ nanoparticles and their enhanced photocatalytic activity for dye degradation. *J. Nanosci. Nanotechnol.* **2016**, *16*, 570–575. [[CrossRef](#)] [[PubMed](#)]
11. Han, C.; Liu, J.; Yang, W.; Wu, Q.; Yang, H.; Xue, X. Photocatalytic activity of CaTiO₃ synthesized by solid state, sol–gel and hydrothermal methods. *J. Sol Gel Sci. Technol.* **2017**, *81*, 806–813. [[CrossRef](#)]
12. Singh, D.; Baitha, P.; Manam, J. Enhancement of luminescence intensity and spectroscopic analysis of Eu³⁺ activated and Li⁺ charge-compensated CaTiO₃ color tunable phosphors for solid-state lighting. *Appl. Phys. A* **2016**, *122*, 668. [[CrossRef](#)]
13. Alammara, T.; Hamma, I.; Warkb, M.; Mudring, A. Low-temperature route to metal titanate perovskite nanoparticles for photocatalytic applications. *Appl. Catal. B: Environ.* **2015**, *178*, 20–28. [[CrossRef](#)]

14. Dong, W.; Bao, Q.; Gu, X.; Zhao, G. Controlled synthesis of flower-like CaTiO₃ and effects of morphology on its photocatalytic activities. *J. Ceram. Soc. Jpn.* **2015**, *123*, 643–648. [[CrossRef](#)]
15. Yang, X.; Mu, Y.; Bai, C.; Xu, W.; Hong, C.; Dai, K.; Cheng, S. A CsPbBr₃ Perovskite Quantum Dot/Graphene Oxide Composite for Photocatalytic CO₂ Reduction. *J. Am. Chem. Soc.* **2017**, *139*, 5660–5663.
16. Yi, Z.; Yi, L.; Kristen, M.; Han, Z.; Eilaf, E. Lead Halide Perovskite Nanocrystals as Photocatalysts for PET-RAFT Polymerization under Visible and Near-Infrared Irradiation. *ACS Macro Lett.* **2020**, *9*, 725–730.
17. Yi, Z.; Yi, L.; Qing, A.; Guan, G.; Lin, Y.; Qi, F.; Xiao, T.; Xiang, Z.; Eilaf, E.; Pulickel, A.; et al. In Situ Synthesis of Lead-Free Halide Perovskite–COF Nanocomposites as Photocatalysts for Photoinduced Polymerization in Both Organic and Aqueous Phases. *ACS Mater. Lett.* **2022**, *4*, 464–471.
18. Jiang, E.; Song, N.; Che, G.; Liu, C.; Dong, H.; Yang, L. Construction of a Z-scheme MoS₂/CaTiO₃ heterostructure by the morphology-controlled strategy towards enhancing photocatalytic activity. *Chem. Eng. J.* **2020**, *399*, 125721. [[CrossRef](#)]
19. Zhang, J.; Zhang, S.; Liu, B. Degradation technologies and mechanisms of dioxins in municipal solid waste incineration fly ash: A review. *J. Clean. Prod.* **2020**, *250*, 119507. [[CrossRef](#)]
20. Yan, Y.; Yang, H.; Zhao, X.; Zhang, H.; Jiang, J. A hydrothermal route to the synthesis of CaTiO₃ nanocuboids using P25 as the titanium source. *J. Electron. Mater.* **2018**, *47*, 3045–3050. [[CrossRef](#)]
21. Kumar, A.; Schuerings, C.; Kumar, S.; Kumar, A.; Krishnan, V. Perovskite-structured CaTiO₃ coupled with g-C₃N₄ as a hetero-junction photocatalyst for organic pollutant degradation. *Beilstein J. Nanotechnol.* **2018**, *9*, 671–685. [[CrossRef](#)] [[PubMed](#)]
22. Ariane, S.; Aldo, J.; Zarbin. Molybdenum-based two-dimensional materials: Synthesis, dispersion, exfoliation and thin film deposition. *J. Colloid Interface Sci.* **2019**, *554*, 80–90.
23. Liu, J.; Mu, X.; Yang, Y. Construct 3D Pd@MoS₂-conjugated polypyrrole/ram works heterojunction with unprecedented photocatalytic activity for Tsuji-Trost reaction under visible light. *Appl. Catal. B Environ.* **2019**, *244*, 355–366. [[CrossRef](#)]
24. Shahid, W.; Idrees, F.; Iqbal, M.; Tariq, M.; Shahid, S.; Choi, J. Ex Situ Synthesis and Characterizations of MoS₂/WO₃ Heterostructures for Efficient Photocatalytic Degradation of RhB. *Nanomaterials* **2022**, *12*, 2974. [[CrossRef](#)]
25. Jiang, Z.; Pan, J.; Wang, B.; Li, C. Two dimensional Z-scheme AgCl/Ag/CaTiO₃ nano-heterojunctions for photocatalytic hydrogen production enhancement. *Appl. Surf. Sci.* **2018**, *436*, 519–526. [[CrossRef](#)]
26. Xiang, Z.; Nan, J.; Deng, J.; Shi, Y.; Zhao, Y.; Zhang, B.; Xiang, X. Uniform CdS-decorated carbon microspheres with enhanced photocatalytic hydrogen evolution under visible-light irradiation. *J. Alloy. Compd.* **2019**, *770*, 886–895. [[CrossRef](#)]
27. Min, C.; Qiang, X.; Zhu, L.; Qiu, K.; Xuan, X. Synthesis and photocatalytic activity of Na⁺ co-doped CaTiO₃:Eu³⁺ photocatalysts for methylene blue degradation. *Ceram. Int.* **2020**, *46*, 12111–12119.
28. Cao, D.; Wang, Q.; Zhu, S.; Zhang, X.; Li, Y.; Cui, Y.; Xue, Z.; Gao, S. Hydrothermal construction of flower-like MoS₂ on TiO₂ NTs for highly efficient environmental remediation and photocatalytic hydrogen evolution. *Sep. Purif. Technol.* **2021**, *265*, 118463. [[CrossRef](#)]
29. Mei, W.; Chen, C.; Liu, X.; Yang, Z.; Ding, F.; Chao, Z.; Liu, T. Low-temperature construction of MoS₂ quantum dots/ZnO spheres and their photocatalytic activity under natural sunlight. *J. Colloid Interface Sci.* **2018**, *530*, 714–724. [[CrossRef](#)]
30. Senthil, R.; Osman, S.; Pan, J.; Sun, Y.; Kumar, T.; Manikandan, A. A facile hydrothermal synthesis of visible-light responsive BiFeWO₆/MoS₂ composite as superior photocatalyst for degradation of organic pollutants. *Ceram. Int.* **2019**, *45*, 18683–18690. [[CrossRef](#)]
31. Deng, B.; Si, P.; Bauman, L.; Luo, J.; Rao, M.; Peng, Z.; Jiang, T.; Li, G.; Zhao, B. Photocatalytic activity of CaTiO₃ derived from roasting process of bauxite residue. *J. Clean. Prod.* **2020**, *244*, 118598. [[CrossRef](#)]
32. Yan, Y.; Yang, H.; Yi, Z.; Xian, T.; Wang, X. Direct Z-scheme CaTiO₃@BiOBr composite photocatalysts with enhanced photodegradation of dyes. *Environ. Sci. Pollut. Res.* **2019**, *26*, 29020–29031. [[CrossRef](#)] [[PubMed](#)]
33. Cui, Z.; Sun, Y.; Zhang, Z.; Xu, M.; Xin, B. Facile synthesis and photocatalytic activity of Ag₃PO₄ decorated MoS₂ nanoflakes on carbon fiber cloth. *Mater. Res. Bull.* **2018**, *100*, 345–352. [[CrossRef](#)]
34. Yu, Y.; Liu, K.; Zhang, Y.; Xing, X.; Li, H. High Photocatalytic Activity of g-C₃N₄/La-N-TiO₂ Composite with Nanoscale Heterojunctions for Degradation of Ciprofloxacin. *Int. J. Environ. Res. Public Health* **2022**, *19*, 4793. [[CrossRef](#)] [[PubMed](#)]

Disclaimer/Publisher's Note: The statements, opinions and data contained in all publications are solely those of the individual author(s) and contributor(s) and not of MDPI and/or the editor(s). MDPI and/or the editor(s) disclaim responsibility for any injury to people or property resulting from any ideas, methods, instructions or products referred to in the content.